# Composition and strain engineered AgNbO3-based multilayer capacitors for ultra-high energy storage capacity

SCHOLARONE™
Manuscripts

# Composition and strain engineered AgNbO$_3$-based multilayer capacitors for ultra-high energy storage capacity

Li-Feng Zhu[1,2], Lei Zhao[3], Yongke Yan[*1], Haoyang Leng[1], Xiaotian Li[1], Li-Qian Cheng[1], Xiangming

Xiong[4], Shashank Priya[*1]

[1] Department of Materials Science and Engineering, The Pennsylvania State University, University Park,

PA 16802, United States

[2] School of Materials Science and Engineering, University of Science and Technology Beijing, Beijing

100083, China.

[3.] College Physics Science & Technology, Hebei University, Baoding 071002, China

[4.] The Program in Applied and Computational Mathematics, Princeton University, Princeton, NJ 08544,

United States

## Abstract

The antiferroelectric (AFE) materials owing to their double-loop-shaped electric-field (E) dependent

polarization (P) are considered quite promising for energy-storage capacitors. Among large family of AFE

materials, AgNbO$_3$ composition, is attractive not only because it is environment-friendly, but also it has high

recoverable energy storage density ($W_{rec}$). However, reported values of $W_{rec}$<4 J/cm$^3$ in Ag(Nb$_{0.85}$Ta$_{0.15}$)O$_3$

multilayer capacitors is lower than that of corresponding monolithic ceramic. This is attributed to high leakage

current density ($J$) and inferior breakdown strength (BDS) in multilayer structures. Here we demonstrate that

MnO$_2$ doping not only effectively reduces the $J$ value and results in slim P-E loops, but also enhances the

breakdown strength (BDS). Multilayer capacitors with composition Ag(Nb$_{0.85}$Ta$_{0.15}$)O$_3$+0.25wt%MnO$_2$

(ANT+Mn) demonstrated an excellent $W_{rec}$=7.9 J/cm$^3$ and efficiency η=71%. Extensive investigations were

---

Corresponding author: yxy355@psu.edu (Yongke Yan)
Corresponding author: sup103@psu.edu (Shashank Priya)
These authors (Li-Feng Zhu, Lei Zhao) contributed equally to this work.

conducted on ANT+Mn multilayer capacitors to demonstrate the role of strain engineering in enhancing the maximum polarization ($P_{max}$) and $\Delta P$ values. Results reveal the role of built-in stress in active layers of multilayer capacitors on the magnitude of $P_{max}$, remanent polarization ($P_r$) and $W_{rec}$, and provide guidance towards the development of high energy storage density in multilayer capacitors.

***Keywords***: Dielectric capacitor; Multilayer capacitors; $AgNbO_3$; Energy storage

# 1. Introduction

Dielectric capacitors provide key advantages, such as high-power density, fast charge/discharge rates, good fatigue resistance and temperature stability. This is attractive for applications in pulsed-discharge and power conditioning for electronic systems, such as hybrid electric vehicles, high-powered accelerators, space shuttle power systems, and kinetic energy weapons [1-6]. However, the energy-storage density ($W$) of dielectric capacitors is much lower than that of batteries or electrochemical capacitors. Theoretically, the $W$ of the dielectric capacitor can be expressed by the integral of the polarization-electric field ($P$-$E$) hysteresis loops [7,8]:

$$W = \int_0^{D_{max}} E dD \approx \int_0^{P_{max}} E dP \qquad (1)$$

$$W_{re} \approx \int_{P_r}^{P_{max}} E dP \qquad (2)$$

$$\eta = \frac{W_{re}}{W} \times 100\% \qquad (3)$$

where $E$, $D$ and $D_{max}$ are the electric field, electric displacement, and maximum electric displacement under the applied electric field. $P$, $P_r$ and $P_{max}$ represent polarization at a given E, remanent polarization, and the maximum polarization. The parameters $W$, $W_{rec}$ and $\eta$ represent total energy storage density, recoverable energy storage density and energy storage efficiency, respectively.

There is continuous emphasis in research and industrial community on simultaneous achievement of a low $P_r$, a high $P_{max}$ and a high breakdown strength (BDS) in multilayer capacitors in order to improve the $W_{rec}$ and $\eta$ [9]. There are various choices for dielectric materials comprising of antiferroelectrics (AFEs) [10-12], relaxor ferroelectrics (RFEs) [13, 14], normal ferroelectrics (FEs) [15]and linear nonpolar dielectric materials[16]. Among these, AFE dielectric capacitors are attractive as they exhibit unique double $P$-$E$ hysteresis loops as a result of electric field induced reversible AFE-FE phase transition. This is beneficial in improving $W_{rec}$, due to relatively high $P_{max}$ and extremely low $P_r$ compared with other types of dielectric capacitors. For example, excellent $W_{rec}$ of 3~11 J/cm³ has been reported in PbZrO$_3$-based AFE ceramics [10,11,17-19].

Considering the adverse effect of lead oxide on the environment and human health, current emphasis is on finding lead-free compositions [20-22]. Among the lead-free ceramics, $AgNbO_3$ system is promising for energy-storage because of its AFE-like hysteresis loops and high saturation polarization (up to 52 $\mu C/cm^2$) [23]. The structure of pure $AgNbO_3$ system is similar to that of other AFE materials. However, it exhibits a weak $P_r$ at room temperature due to its ferrielectric behavior, which has a negative impact on the energy storage performance of $AgNbO_3$ ceramics. For example, the $W_{rec}$ of unmodified $AgNbO_3$ ceramic is ~2 $J/cm^3$[24,25], which is far lower than that of $PbZrO_3$-based AFE systems [17-19]. Recently, most of the research efforts have focused on suppressing the ferrielectricity and boosting the antiferroelectricity, through various modifications: (1) adding dopant oxides, e.g., $MnO_2$,[26], $WO_3$,[27] etc.; and (2) ion substitutions, e.g., replacement of $Ag^+$ by $La^{3+}$[28], $Sm^{3+}$[29], $Ba^{2+}$[30], $Lu^{3+}$[31], $Gd^{3+}$[32], etc., and/or $Nb^{5+}$ by $Ta^{5+}$ [33]. The $W_{rec}$ of $AgNbO_3$ ceramic increases from 2 $J/cm^3$ [24,25] to 2.5 $J/cm^3$ in $AgNbO_3$+0.1wt%$MnO_2$ system[26], 3.3 $J/cm^3$ in $AgNbO_3$+0.1wt%$WO_3$ system[27], 3.2 $J/cm^3$ in $Ag_{1-3x}La_xNbO_3$ system at $x$=0.02[28], 4.5 $J/cm^3$ in $Ag_{1-3x}Sm_xNbO_3$ system at $x$=0.02[29], 2.3 $J/cm^3$ in $Ag_{1-2x}Ba_xNbO_3$ system at $x$=0.02[30], and 4.2 $J/cm^3$ in $Ag(Nb_{1-x}Ta_x)O_3$ system at $x$=0.15[33]. Most of the other studies in literature have also reported $W_{rec}$ values that is in the range of 2 to 4.5 $J/cm^3$. These improvements in $W_{rec}$ have indicates the promise of $AgNbO_3$ ceramics for energy storage application, but also indicates the need to find strategies for further improving $W_{rec}$ and $\eta$.

Multilayer ceramic capacitors (MLCCs), as shown in Fig.1a, have received extensive attention in energy storage areas because they possess advantage in achieving high BDS and low field drive [34]. The BDS of multilayer ceramic capacitor prepared by tape casting can be enhanced to more than three times in comparison to the monolithic ceramic capacitor. For example, the BDS of $0.61BiFeO_3$-$0.33(Ba_{0.8}Sr_{0.2})TiO_3$-$0.06La(Mg_{2/3}Nb_{1/3})O_3$ multilayer capacitors is up to 730 kV/cm, which is far higher than 230 kV/cm for ceramics bulk. Due to this increase in BDS, the $W_{rec}$ of $0.61BiFeO_3$-$0.33(Ba_{0.8}Sr_{0.2})TiO_3$-$0.06La(Mg_{2/3}Nb_{1/3})O_3$ multilayer capacitors is about 3 times as high as ceramics bulk [35]. In addition to high

BDS of over 700 kV/cm, an excellent $W_{rec}$=10.5 J/cm$^3$ has been achieved in (0.7-$x$)BiFeO$_3$-0.3BaTiO$_3$-$x$Nd(Zn$_{0.5}$Zr$_{0.5}$)O$_3$ multilayer capacitors [36]. Hence, it is expected that a higher $W_{rec}$ will be achieved in AgNbO$_3$ multilayer capacitors. However, to the best of our knowledge, there is no reported success in demonstrating the AgNbO$_3$ multilayer capacitors with high W$_{rec}$. The reason could be related to presence of large strain during synthesis which arises from volume variation caused by AFE-to-FE transformation [37] as shown in Fig.1b and 1c. A large strain will cause a lower BDS, which was reported in nontextured NBT-SBT multilayer capacitor, comparing with the <111> textured sample [21].
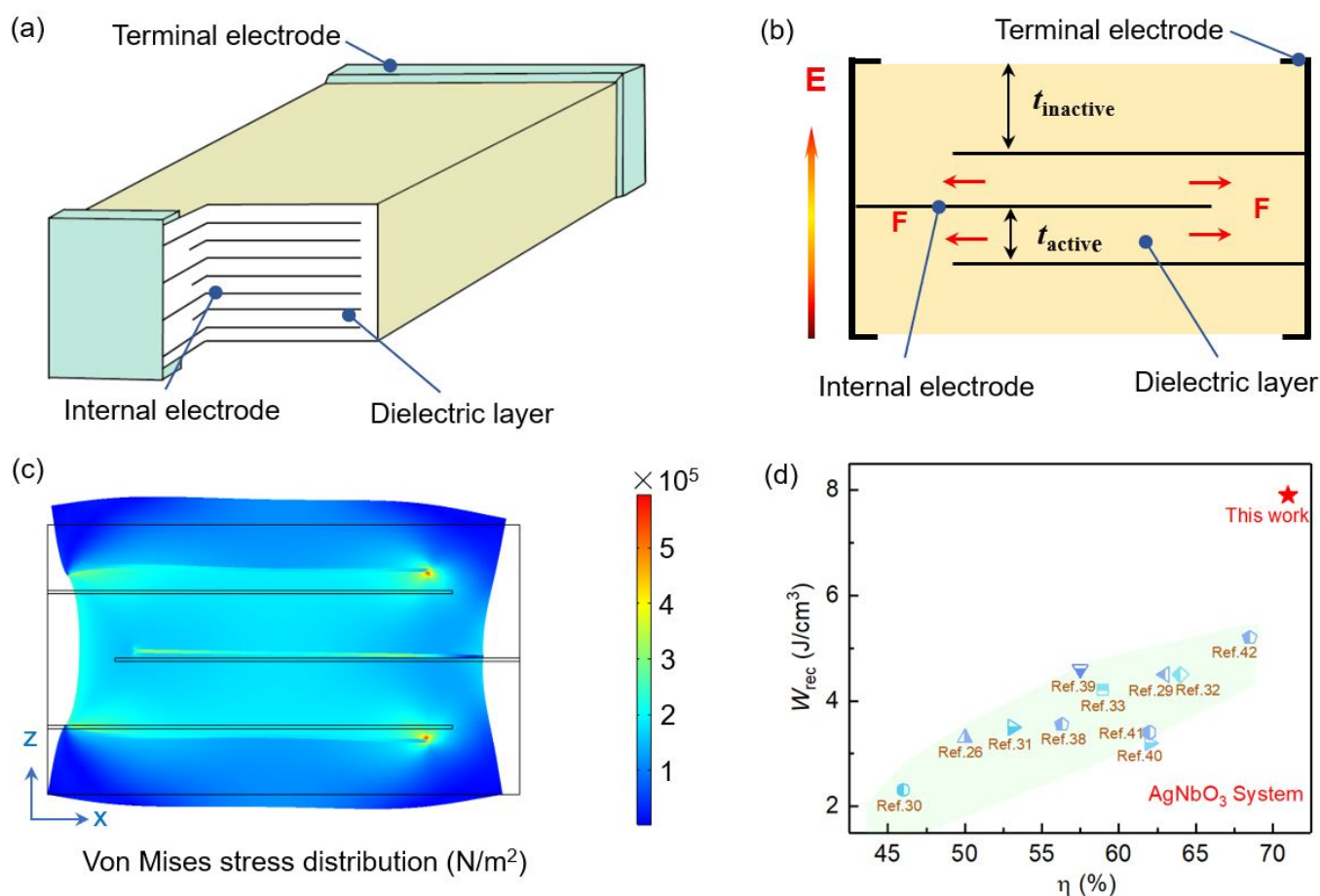


Figure 1. Schematics of (a) a MLCC, and (b) the strain distribution in cross-section of a MLCC when it was exposed to a high electric field. Here, $t_{inactive}$ is the thickness of inactive dielectric ceramic layer, $t_{active}$ is the thickness of active dielectric ceramic layer, and $F$ is the force exerted on the active dielectric ceramic layer by the clamping from inactive layer. (c), Finite-element simulations for the distribution of strains with application of 10 V between two electrodes. (d) Review of the recoverable energy storage densities ($W_{re}$) and energy efficiency ($\eta$) reported for AgNbO$_3$ based energy storage materials [26, 29-33, 38-42].

$Ag(Nb_{0.85}Ta_{0.15})O_3$ multilayer capacitors were synthesized and their energy-storage densities were investigated. An inferior $W_{rec}$ was found in $Ag(Nb_{0.85}Ta_{0.15})O_3$ multilayer capacitor because of its high leakage current density ($J$) and low breakdown strength (BDS). On modification with $MnO_2$, there is significant improvement in the $J$ and BDS, and an excellent energy-storage performance with $W_{rec} = 7.9$ J/cm$^3$ and η=71% is achieved in $Ag(Nb_{0.85}Ta_{0.15})O_3$+0.25wt%$MnO_2$ (ANT+Mn) multilayer capacitors. To the best of our knowledge, these $W_{rec}$ and η values of $Ag(Nb_{0.85}Ta_{0.15})O_3$+0.25wt%$MnO_2$ capacitors are the highest reported values in $AgNbO_3$ system, as shown in Fig. 1d. Experimental and modeling results reported here provide a systematic approach for enhancing the $W_{rec}$ of $AgNbO_3$ based multilayer capacitors.

## 2. Experimental

Silver oxide ($Ag_2O$, 99.7%), Niobium pentoxide ($Nb_2O_5$, 99.99%), tantalum oxide ($Ta_2O_5$, 99.99%), and manganese dioxide ($MnO_2$, 99.0%) were used as raw materials. These powders were weighed according to the composition, $Ag(Nb_{0.85}Ta_{0.15})O_3$ (ANT), and mixed in ethanol. The mixture was dried, pressed, and calcined at 900 °C for 5 h in an oxygen atmosphere. The resultant pellets were meshed and remixed for further processing. The MLCC samples were prepared by the tape-casting and cofiring method. To obtain a suitable slurry, the milled ANT and $Ag(Nb_{0.85}Ta_{0.15})O_3$+0.25wt% $MnO_2$ (ANT+Mn) ceramic powders (56 wt%) were mixed with a solution of Xylene (17 wt%), ethanol (17 wt%), menhaden fish oil (1.2 wt%), polyethylene glyco 400 (1.5 wt%), butyl benzyl phthalate (1.5 wt%) and Polyvinyl Butyral (PVB, 3wt%). This mixture was ball-milled for 24 h. Tape casting was performed using laboratory-type tape-casting machine with a doctor blade casting head (100 μm opening), using 75 μm thick silicone-coated mylar (polyethylene terephthalate) as a carrier film. The green tapes were cut into square samples of 1-inch in length. Layers of ANT and ANT+Mn green tapes were stacked and laminated using a uniaxial hot press at 70 °C to achieve a single thick dielectric layer. Pt paste was screen-printed as an internal electrode on top of the dielectric layer. Screen-printed layers were stacked and laminated to form MLCCs.

Ferroelectric hysteresis loops were measured using 10 kV HVI-SC precision materials analyzer (Radiant

technologies INC, USA). The microstructure of the multilayer capacitors was evaluated using field-emission scanning electron microscopy (FESEM Apreo) in combination with energy dispersive spectroscopy (EDS). TEM images were collected by FEI Titan3 G2 double aberration-corrected microscope at 300 kV. EDS elemental maps of the sample were collected by using a SuperX EDS system under STEM mode. The TEM sample was prepared by focused ion beam (FIB, FEI Helios 660) lift-out technique. The temperature dependence of dielectric properties was examined using a programmable furnace with an E4980AL Precision LCR Meter at 1 kHz in a temperature range of 23 °C to 560 °C. Impedance spectroscopy was performed using an Agilent E4980A impedance AC analyzer (Agilent Technologies Inc., Palo-Alto, CA) and impedance data was collected from 300 to 550 °C at 25 °C intervals on heating. Impedance data were normalized by a geometric factor (thickness/surface area). The Comsol5.5 software was used to finite-element simulations, in which the length and width of 3D model are 6 mm and 4.5 mm, respectively. The terminal voltages in the bottom Pt electrode were set $V_1$ which is equal to $E_1 * t_{active}$. The terminal voltages in the top Pt electrode were set 0 V.

## 3. Results and discussion

### 3.1 Energy-storage performance of ANT multilayer capacitors

Figure 2a shows the *P-E* loops for ANT multilayer capacitors with different active thickness. All samples exhibit typical antiferroelectric P-E loops. However, as the thickness of active layers ($t_{active}$) reduces, from 68 μm to 17 μm, the remnant polarization ($P_r$) increases and $P_{max}$ decreases. These trends are unfavorable towards enhancing the energy storage density. Fig. 2b shows the Weibull breakdown strength of ANT multilayer capacitors. With decreasing $t_{active}$, the BDS of the capacitors increases and reaches to 600 kV/cm as $t_{active}$=17 μm. Although the BDS for capacitor is higher at $t_{active}$=17 μm, its recoverable energy storage ($W_{rec}$) value is the lowest among all ANT multilayers capacitors and presents a decreasing trend when the electric field is over 300 kV/cm as shown in Fig. 2c. This phenomenon, where $W_{rec}$ first increases and then decreases when the electric field increases from 100 kV/cm to 450 kV/cm is also found in capacitors with $t_{active}$=34 μm.

However, this trend disappears as $t_{active}$ rises over 51 μm. The deterioration of $W_{rec}$ in the capacitors of $t_{active}$=17

μm and 34 μm when the measurement electric field is over 300 kV/cm, may be due to the high leakage current

density caused by volatilization of Ag or reduction of Ag ions. This high leakage current density is reflected

by round $P$-$E$ loops as shown in Fig. 2d and Fig. S1a. For $P$-$E$ measurement using Sawyer-Tower circuit, the

polarization is determined by the charge arising from the ferroelectric switching current based on the

assumption of ideal capacitive ferroelectric samples. In high leakage sample, the apparent remanent

polarization value $P_{r,\,apparent}$ from $P$-$E$ measurement combines with the real remanent ferroelectric polarization

from ferroelectric switching current and the accumulated charge polarization from the leakage current. As

shown in Fig. 2e, the value of $P_{r,\,apparent}$ for sample at $t_{active}$=17 μm increases sharply with increasing the electric

field. As the measured electric field increases from 100 kV/cm to 600 kV/cm, the $P_{r,\,apparent}$ increases from 0.14

μC/cm² to 32.12 μC/cm². The variation of leakage current density ($J$) of capacitors at $t_{active}$=17 μm is shown

in Fig. 2f. When the electric field reaches to 400 kV/cm, the $J$ of capacitors with $t_{active}$=17 μm is found to be

$8*10^{-4}$ A/cm. Such high $J=8*10^{-4}$ A/cm for the capacitors at $t_{active}$=17 μm as the electric field equals to 400

kV/cm is negative for the improvement of $W_{rec}$ and η.



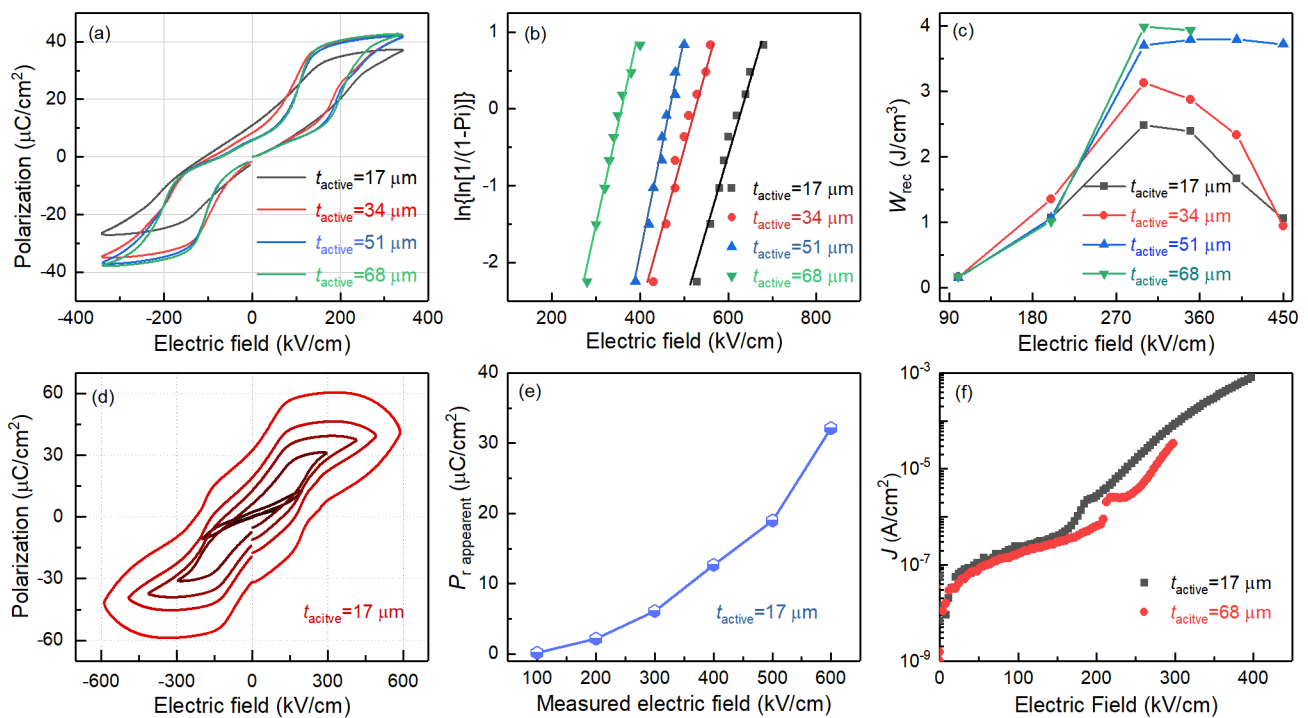Figure 2 (a) $P$-$E$ loops measured at 350 kV/cm, (b) breakdown field and (c) recoverable energy storage $W_{rec}$ for

$Ag(Nb_{0.85}Ta_{0.15})O_3$ multilayer capacitors, where the $t_{active}$ is 17 μm, 34 μm, 51 μm and 68 μm, respectively, (d) *P-E* loops for the samples with $t_{active}$=17 μm, measured at different electric field, (e) apparent remanent polarization, $P_{r,apparent}$, obtained from the *P-E* loops, and (f) leakage current density *J* for samples with $t_{active}$=17 μm and 68 μm.

## 3.2 Improving resistance of ANT multilayers capacitors via MnO₂ doping

Based on the above results, the BDS of ANT multilayer capacitors can be enhanced by decreasing $t_{active}$, but the energy storage performance is not satisfactory. The main problem is related to a high leakage current density, that appears in the capacitor at $t_{active}$=17 μm when the applied electric field is over 300 kV/cm. In order to overcome this drawback, we investigated enhancement in the resistance of capacitors via introduction of $MnO_2$. Figure 3a shows the *P-E* loops of ANT multilayers capacitors, with and without doping $MnO_2$, measured at 450 kV/cm. It can be observed that the ANT multilayers capacitors with $MnO_2$ doping (ANT+Mn) have a slim *P-E* loop, suggesting that the $MnO_2$ doping significantly improves the energy storage performance. Fig. 3b exhibits the leakage current of ANT multilayers capacitors with and without doping $MnO_2$. Compared to the unmodified ANT sample, a small addition of $MnO_2$ can effectively decrease the leakage current of ANT capacitors. A low leakage current density $J$=2.5*$10^{-6}$ A/cm² is observed at 500 kV/cm in ANT+Mn capacitor, suggesting that $MnO_2$ doping will improve the resistance of ANT multilayers. The impedance spectroscopy data for ANT capacitors further verifies that the resistance of ANT+Mn capacitors was enhanced by doping $MnO_2$ as shown in Fig.3c. The variation of dielectric constant and dielectric loss as a function of temperature for ANT capacitors with doping and undoping $MnO_2$ are shown in Fig.3d. The dielectric curves of both capacitors almost overlap and three phase transition peaks, corresponding to $M_2$-$M_3$, $M_3$-O and O-T, respectively, occur at 223 °C, 350 °C and 395 °C. $M_2$ and $M_3$ are antiferroelectric phases, while O and T are paraelectric phases. These results indicate that a small amount of $MnO_2$ doping has no effect on the dielectric constant and phase-transition temperatures. However, compared with unmodified ANT capacitor, the dielectric loss of ANT+Mn capacitor reduces, especially as the temperature rises above 250 °C the decrease in dielectric loss is more evident, as shown in Fig3d. Hence, we can conclude that $MnO_2$ doping has positive

effect on improving the resistance, BDS, efficiency (η) and energy storage density of ANT multilayer capacitors.
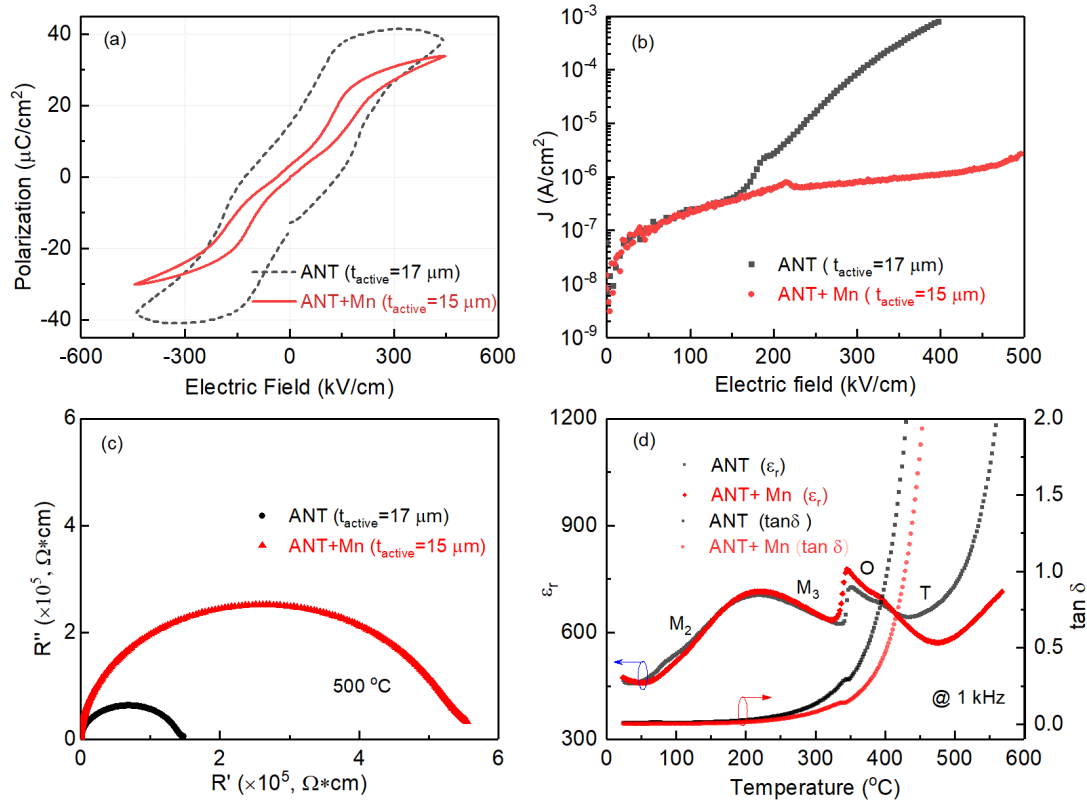


Figure 3 Effect of $MnO_2$ doping on *P-E* loops, leakage current, resistance and dielectric properties of ANT capacitors. (a) *P-E* loops measured at 450 kV/cm; (b) leakage current *J*, (c) temperature dependence of dielectric constant $\varepsilon_r$ and dielectric loss tan$\delta$, and (d) impedance spectroscopy measured at 500 °C for ANT and ANT+Mn capacitors.

## 3.3 Effect of clamping stress on the *P-E* loop of ANT+Mn multilayer capacitor

Besides material composition, stress is important factor affecting the *P-E* loops, especially in ferroelectric thin film which suffer from large clamping stresses from substrate [43,44]. As shown in Fig. 1, outside inactive layers clamp the deformation of active dielectric layers in MLCC under applied electric field. Due to large strain caused by phase transition between AFE to FE phases or electrostriction, the clamping stress due to the inactive layer may have a significant impact on *P-E* loops and energy storage performance of active dielectric layers. In order to investigate this effect, one-layer capacitors with fixed $t_{active}$=22 μm and varying $t_{inactive}$ were designed. The schematic structure is shown in Fig. 4a. The results show that as the $t_{inactive}$ increases, the $P_{max}$ value decreases while $P_r$ value remains unchanged in ANT+Mn capacitor, as shown in Fig.4b. This result

reveals that the stress originating from the clamping of inactive layer has impact on the AFE-to-FE phase transformation and ferroelectric domain switching. Detailed variations of $P_{max}$, $P_r$, and $\Delta P$ as a function of $t_{inactive}$ for ANT+Mn capacitor are shown in Fig. 4c. Under applied field of 400 kV/cm, as the $t_{inactive}$ increases from 33 μm to 165 μm, the value of $P_{max}$ and $\Delta P$ with magnitude of 34.8 μC/cm$^2$ and 32.8μC/cm$^2$ is found to decrease to 28.6 μC/cm$^2$ and 26.7μC/cm$^2$. This phenomenon can be explained that the domain alignment was suppressed. The reduction in $P_{max}$ and $\Delta P$ as the $t_{inactive}$ increases, results in the decrease of the $W_{total}$ and $W_{rec}$, as shown in Fig.S2a. The $W_{rec}$ decreases from 5.6 J/cm$^3$ at $t_{inactive}$= 33 μm to 4.7 J/cm$^3$ at $t_{inactive}$= 165 μm, slightly over 15% decline.

To clarify the effect of stress on the $P_{max}$ and $W_{rec}$, finite-element simulations were performed as shown in Fig.4d-f. As the $t_{inactive}$ increases, the stress in the active layer also increases. The variation of average stress of active layer as a function of $t_{inactive}$ is shown in Fig.4g. With increasing $t_{inactive}$, the average stress of active layer increases, contrary to the variation of $P_{max}$ and $W_{rec}$ of capacitors. This result indicates that the reason making the domain alignment suppressed and the $P_{max}$ decreased is the stress which comes from the inactive layer clamping. The larger stress in active layer, the more difficult for domain switching and the lower $P_{max}$ under the same electric field. This phenomenon is also detected in Ref 45, where the saturation polarization shows a significant decrease with the increase of compressive pre-stress in soft PZT ceramic during loading. The results were explained by noting that the applied stress tends to maintain the ferroelectric domain alignment along their polar axes away from the stress direction through the non-180∘ ferroelectric domain switching processes. Therefore, it will require a larger than usual applied electric field to reorient the domains along the stress direction, resulting in a lower value of the saturated polarization [45]. For ANT+Mn multilayer capacitor, the clamping stress derived from the inactive layer suppresses the $x$ and $y$-direction shrinkage and $z$-direction expansion of active layer as shown in Fig 1c. Thus, it also has a negative effect on the non-180∘ ferroelectric domain switching process. When the clamping stress increases the reorientation of the non-180∘ ferroelectric domain will be difficult, causing the decrease of $P_{max}$, $\Delta P$ and $W_{rec}$ of ANT+Mn capacitor.
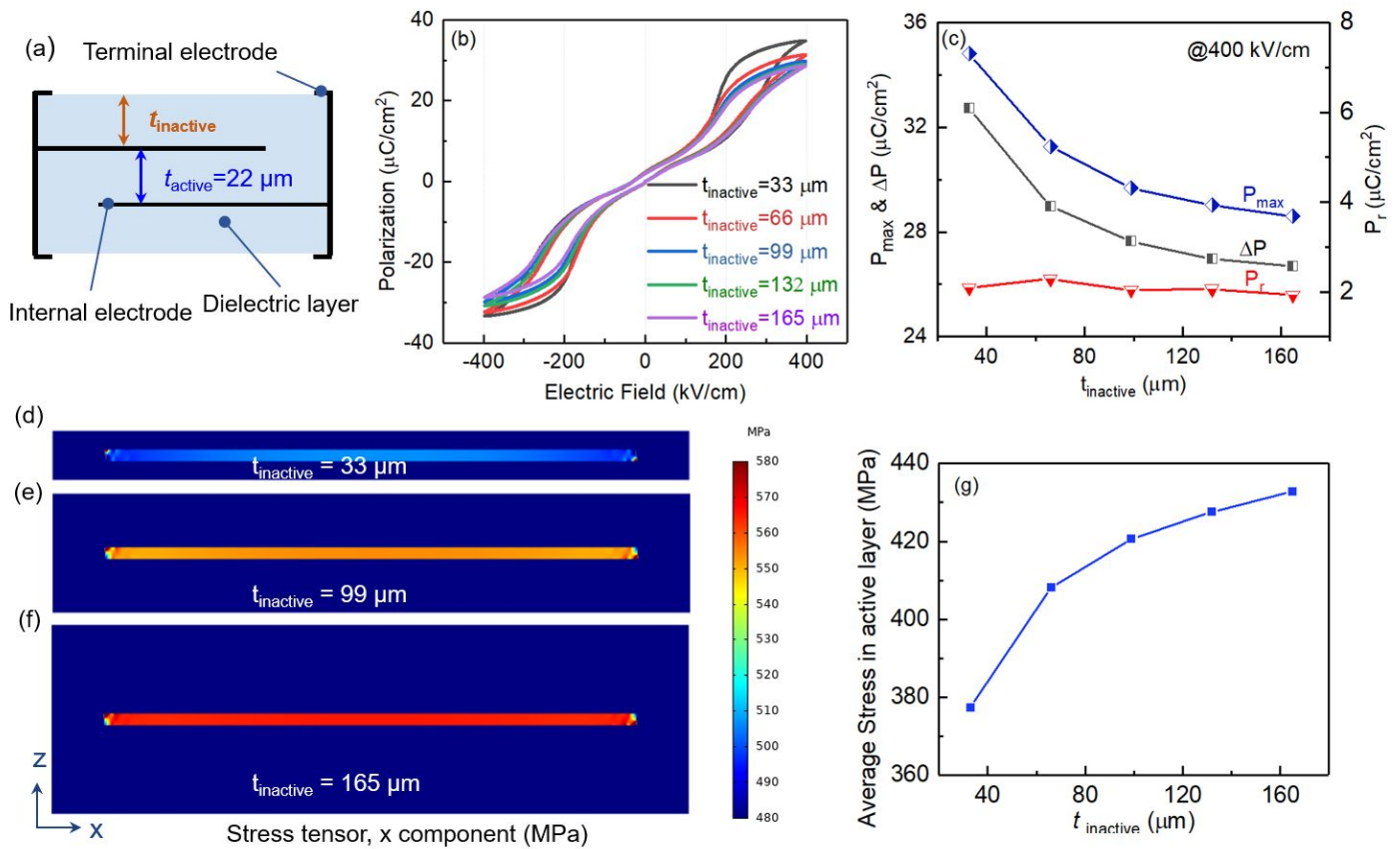
Figure 4. Effect of $t_{inactive}$ on the P-E loop and energy storage density, (a) schematic of ANT+Mn capacitors where the $t_{active}$ was fixed at 22 μm; (b) P-E loop of ANT+Mn capacitors with different $t_{inactive}$; (c) the variation of $W_{rec}$ and $P_{max}$ as a function of $t_{inactive}$ for ANT+Mn capacitor; (d-f) the finite-element simulations, where the electric field between two electrodes is 250 kV/cm, and (g) the variation of average stress of active layer as a function of $t_{inactive}$.

To further reveal the relationship between the clamping stress and $P_{max}$ or $P_r$, the capacitors with varying $t_{active}$ and fixed $t_{inactive} = 33$ μm were designed, as shown in Fig.5a. With increasing $t_{active}$, the $P_{max}$ increases as shown in Fig. 5b. This phenomenon is consistent with the $P\text{-}E$ loop result of unmodified ANT as shown in Fig.2a. The detailed variations of $P_{max}$, $P_r$, and $\Delta P$ are shown in Fig.5c. They all show monotonic increase with increasing $t_{active}$, especially $P_{max}$. This behavior is opposite to the variation of the stress along $x$-axis which exhibits monotonic decrease when $t_{active}$ increases, as shown in Fig.5d-g. This result further illustrates that the strong clamping stress is detrimental in design of the high energy storage multilayer capacitor. It can be concluded that it is beneficial to reduce the $P_r$, and enhance the $P_{max}$, $W_{rec}$ and η by decreasing the clamping stress, for example, reducing the thickness of inactive layer or increasing the thickness of active layer.
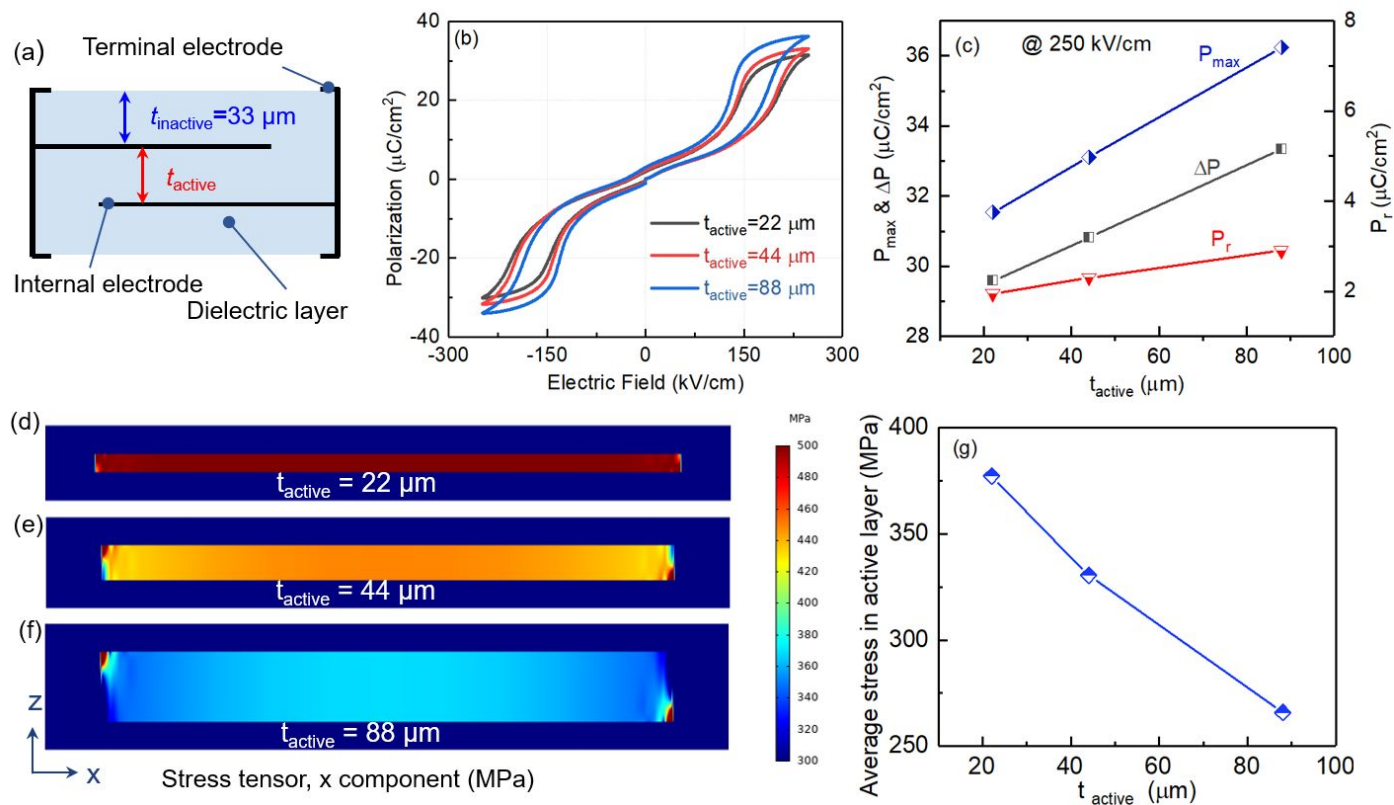
Figure 5. Effect of $t_{active}$ on the P-E loop and energy storage density, (a) schematic of ANT+Mn capacitors where the $t_{inactive}$ was fixed at 33 µm; (b) P-E loop of ANT+Mn capacitors with different $t_{active}$; (c) the variation of $W_{rec}$ and $P_{max}$ as a function of $t_{active}$ for ANT+Mn capacitor; (d-f) finite-element simulations (all active layers are under 250 kV/cm), and (g) the variation of average stress of active layer as a function of $t_{active}$.

## 3.4 Microstructure and energy-storage performance of ANT+Mn multilayer capacitor

Based on above discussions, several MLCC structural factors play role in governing the magnitude of polarization change $\Delta P$ and energy storage density $W_{rec}$: (1) thin inactive layer $t_{inactive}$ (lower volume percentage of active layer) is preferred in order to reduce the clamping stress exerted on active dielectric layers; (2) thin active layer $t_{active}$ is preferred for increasing the BDS; (3) increased number of active layers is required to increase the percentage of active volume in multilayer ceramic capacitors and reduce the clamping stress from inactive layers. Based on these considerations, we synthesized the ANT+Mn multilayer capacitor, where both the inactive and active layers were 15 µm. This configuration is expected to provide a high BDS and low strain. Fig. 6a present the optical image and the size of sample (length × width × height) is 6 × 4.5 × 0.8 mm. The detailed morphologies of the ANT+Mn multilayer capacitor are shown in Figure 6. It can be found that

both the Pt layers and ANT+Mn layers are well crystalized with high density. The grain size in the ANT+Mn layers is less than 2μm as shown in Fig.7a. Fig. 7b shows the high-resolution electron microscopy (HREM) image and the selected-area electron diffraction (SAED) pattern of ANT+Mn layers. The red arrow indicates the (003) reflection. In general, the (00l) reflections with $l = 2n + 1$, provide evidence for the existence of the polar phase with space group Pmc21. The Pmc21 polar phase in the nonpolar matrix accounts for the ferrielectric behavior with nonzero $P_r$ at room temperature [29]. The EDS of micro zone is shown in Fig. 7d, which illustrates the homogeneous distribution of Ag, Nb, Ta and Mn elements across microstructure. There is no segregation of the elements observed in the synthesized ANT+Mn multilayer capacitors.

Due to fine grain size, low leakage current, and small thickness ($t_{active}$=15 μm), an ultra-high BDS of 1020 kV/cm is achieved in ANT+Mn multilayer capacitor, as shown in Fig. 8a. In addition, a large $P_{max}$=43.7 μC/cm$^2$ is achieved by designing thin inactive layer to reduce the clamping stress, as shown in Fig. 8a. Owing to ultra-high BDS=1020 kV/cm and large $P_{max}$=43.7 μC/cm$^2$, an $W_{rec}$ of 7.9 J/cm$^3$ is achieved in ANT+Mn multilayer capacitors. This is highest reported value in AgNbO$_3$ system and is twice that of pure ANT capacitors. The stability of W$_{rec}$ in terms of temperature and frequency dependence is shown in Fig. 8(c-f). $W_{rec}$ of ANT+Mn multilayer capacitor shows excellent temperature stability with fluctuation as low as 3% within the temperature range of room temperature to 100 °C, as shown in Fig. 8c, 8d and Fig S3. The frequency stability of ANT+Mn multilayer capacitor is evaluated by measuring the P-E loops in frequency range between 0.1 and 100Hz, as shown in Fig. 8e. The $W_{rec}$ and η of ANT+Mn multilayer capacitor show slight variation with increasing frequency, as shown in Fig. 8f. These results suggest that ANT+Mn multilayer capacitor is highly promising dielectric capacitor for pulsed-discharge and power conditioning units in electronic systems.
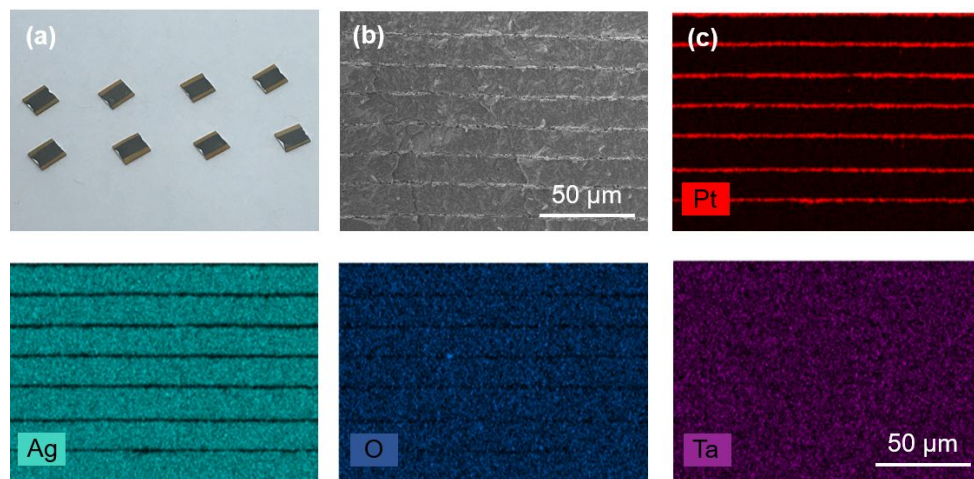
Fig. 6.    Image and microstructures of ANT+Mn multilayer ceramic capacitor. a) Optical photo of the as-prepared ANT+Mn multilayer ceramic capacitors (size of the capacitor: length × width × height=6 × 4.5 ×0.8 mm). b) Cross-sectional SEM image of the MLCC, and (c) EDS-SEM images for the elemental distributions (Pt, Ag, O and Ta).
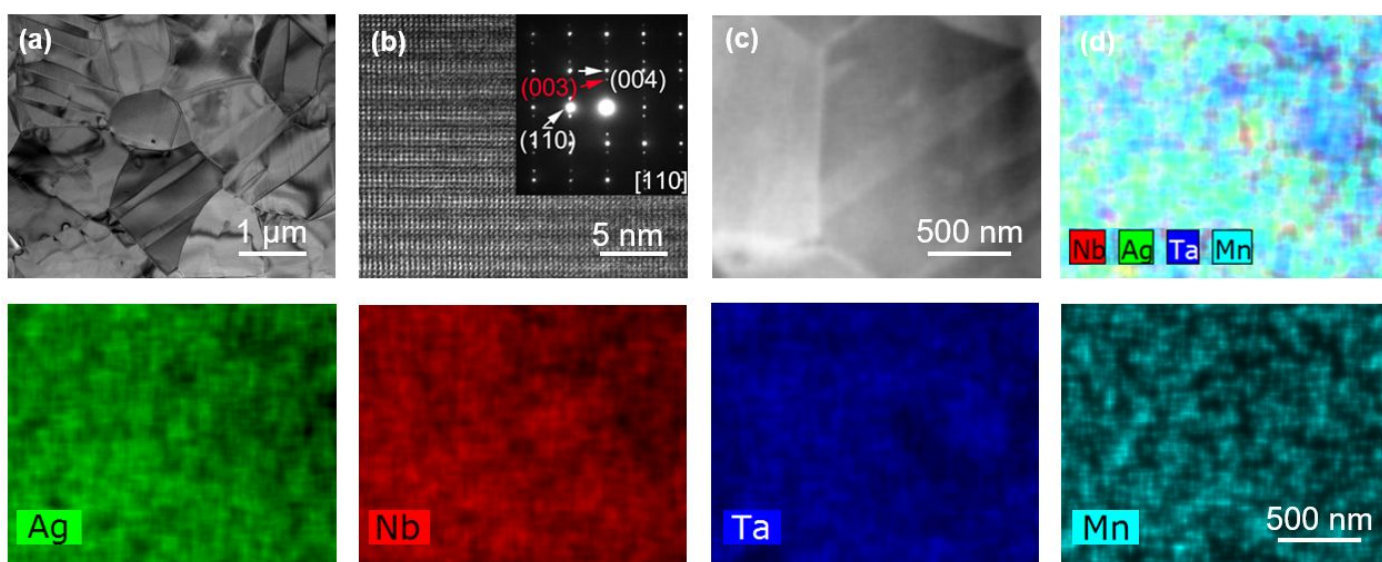


Fig. 7. TEM images of ANT+Mn multilayer capacitor: (a) Microstructure showing grains and grain boundaries. (b) High resolution electron microscopy (HREM) image and selected-area electron diffraction (SAED) pattern (insert), (c) EDS-TEM images for the distributions of specific elements (Ag, Nb, Ta and Mn).
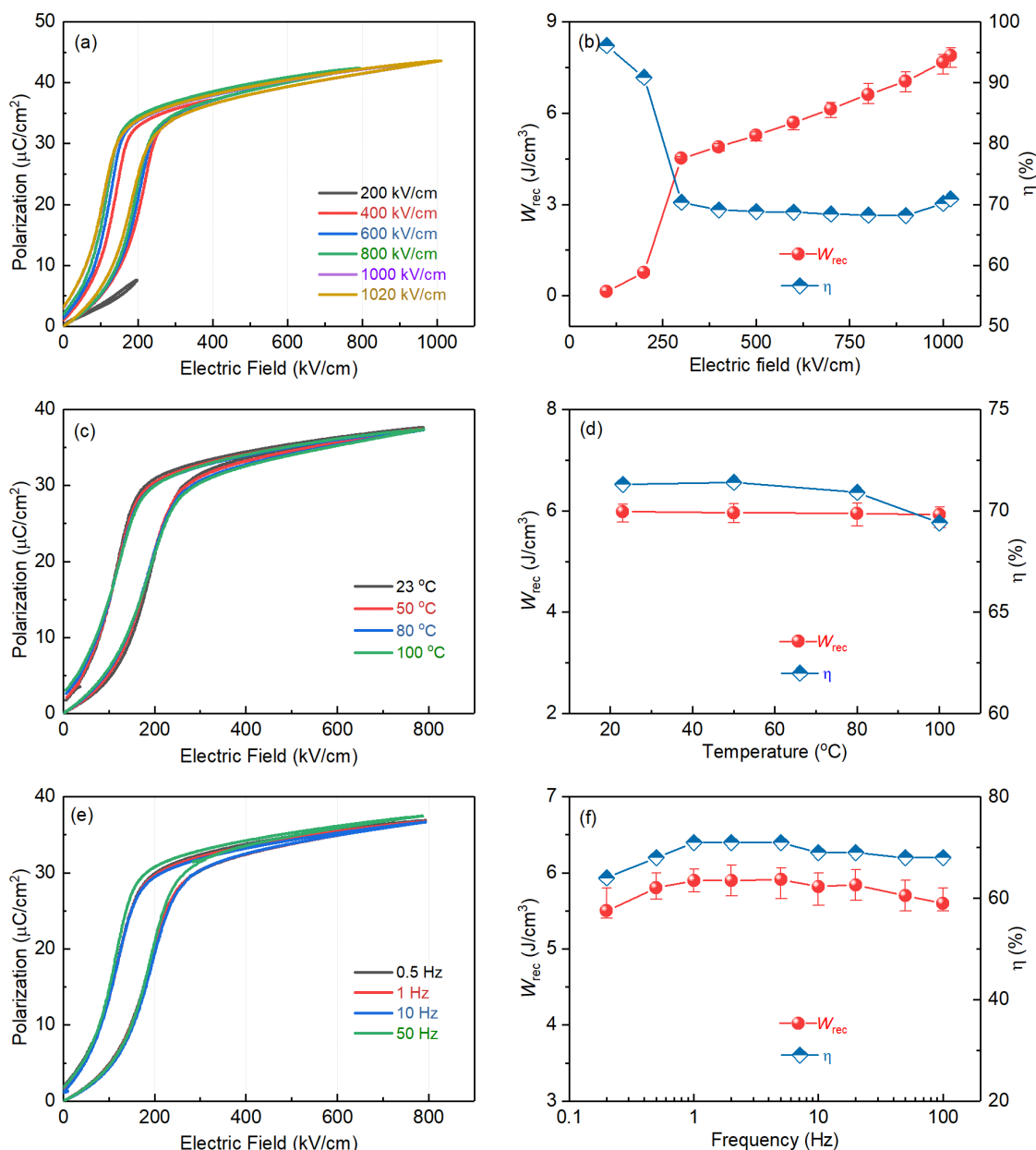
Fig.8. Energy storage of ANT+Mn multilayer capacitors. (a) P-E loops of ANT+Mn multilayer capacitor which can endure a high electric field of 1020 kV/cm, (b) P-E loops of ANT+Mn multilayer capacitor.

## Conclusions

AgNbO$_3$ based multilayer capacitors were synthesized by tape-casting method and its $W_{rec}$ and $\eta$ were tailored through composition and strain engineering. MnO$_2$ doping effectively reduces the leakage and increases the breakdown strength (BDS) of Ag(Nb$_{0.85}$Ta$_{0.15}$)O$_3$ multilayer capacitor. The decrease of stress in active layer for Ag(Nb$_{0.85}$Ta$_{0.15}$)O$_3$+0.25wt%MnO$_2$ (ANT+Mn)capacitor results in increase of the P$_{max}$ and $\Delta$P value. Due

to the low leakage current, ultra-high BDS of 1020 kV/cm, $P_{max}$=43.7 μC/cm$^2$, and $W_{rec}$=7.9 J/cm$^3$ is obtained. This is the highest value of $W_{rec}$ in AgNbO$_3$ system with high efficiency η=71%. These results provide a promising direction for enhancing the energy storage density of ceramic multilayer capacitor.

## Acknowledgments

## References

[1] C.A. Randall, H. Ogihara, J.R. Kim, G.Y. Yang, C.S. Stringer, S. Trolier-McKinstry, M. Lanagan, *In Proceedings of the Pulsed Power Conference*, Washington, DC, USA, **2009**; 346–351.

[2] Prateek, V.K. Thakur, R.K. Gupta, *Chem. Rev.*, **2016**, 116(7), 4260-4317.

[3] Q. Li, F.Z. Yao, Y. Liu, G. Zhang, H. Wang, Q. Wang, *Annu. Rev. Mater. Res.,* **2018**, 48, 219-243.

[4] Z. Yao, Z. Song, H. Hao, Z. Yu, M. Cao, S. Zhang, M.T. Lanagan, H. Liu, *Adv. Mater.*, **2017**, 29(20), 1601727.

[5] H. Palneedi, M. Peddigari, G.T. Hwang, D.Y. Jeong, J. Ryu, *Adv. Funct. Mater.* **2018**, 28, 1803665

[6] F.Z. Yao, Q. Yuan, Q. Wang, H. Wang, Nanoscale, **2020**,12, 17165-17184

[7] B. Peng, Q. Zhang, X. Li, T. Sun, H. Fan, S. Ke, M. Ye, Y. Wang, W. Lu, H. Niu, J.F. Scott, X. Zeng, H. Huang, *Adv. Electron. Mater.*, **2015**, 2015, 1500052.

[8] B. Li, Q.X. Liu, X.G. Tang, T.F. Zhang, Y.P. Jiang, W.H. Li, J. Luo, *RSC Adv.*, **2017**, 7, 43327-43333.

[9] N.H. Fletcher, A.D. Hilton, B.W. Ricketts, *J. Phys. D: Appl. Phys.,* **1996**, 29, 253-258.

[10] P. Gao, Z. Liu, N. Zhang, H. Wu, A.A. Bokov, W. Ren, Z.G. Ye, *Chem. Mater.*, **2019**, 31, 979-990.

[11] X.K. Wei, C.L. Jia, H.C. Du, K. Roleder, J. Mayer, R. E. Dunin-Borkowski, *Adv. Mate*r., **2020**, 32(9), 1907208.

[12] J. Li, F. Li, Z. Xu, S. Zhang, *Adv. Mater.*, **2018**, 30(32), 1802155

[13] N. Liu, R. Liang, Z. Zhou, X. Dong, *J. Mater. Chem. C*, **2018**, 6, 10211-10217.

[14] P. Zhao, H. Wang, L. Wu, L. Chen, Z. Cai, L. Li, X. Wang, *Adv. Energy Mater.*, **2019**, 9, 1803048

[15] L.F. Zhu, X.W. Lei, L. Zhao, M.I. Hussain, G.Z. Zhao, B.P. Zhang, *Ceram. Int.*, **2019**, 45, 20266–20275.

[16] B. Luo, X. Wang, E. Tian, H. Song, H. Wang, L. Li, *ACS Appl. Mater. Interfaces*, **2017**, 9, 19963−19972

[17] S.I. Shkuratov, J. Baird, V.G. Antipov, S. Zhang, J.B. Chase, *Adv. Mater.* **2019**, 31, 1904819.

[18] L. Chen, N. Sun, Y. Li, Q. Zhang, L. Zhang, X. Hao, *J. Am. Ceram. Soc.*, **2018**, 101, 2313–2320.

[19] Q. Zhang, Y. Dan, J. Chen, Y. Lu, T. Yang, X. Yao, Y. He, *Ceram. Int.*, **2017**, 43, 11428–11432

[20] H. Pan, J. Ma, J. Ma, Q. Zhang, X. Liu, B. Guan, L. Gu, X. Zhang, Y.J. Zhang, L. Li, Y. Shen, Y.H. Lin, C.W. Nan, *Nat. Commun.*, **2018**, 9, 1813.

[21] J. Li, Z. Shen, X. Chen, S. Yang, W. Zhou, M. Wang, L. Wang , Q. Kou, Y. Liu, Q. Li, Z. Xu, Y. Chang, S. Zhang, F. Li, *Nature Materials*, **2020**, 19, 999-1005.

[22] H. Pan, F. Li, Y. Liu, Q. Zhang, M. Wang, S. Lan, Y. Zheng, J. Ma, L. Gu, Y. Shen, P. Yu, S. Zhang, L.Q. Chen, Y.H. Lin, C.W. Nan, *Science,* **2019**, 365, 578–582.

[23] D. Fu, M. Endo, H. Taniguchi, T. Taniyama, M. Itoh, *Appl. Phys. Lett.,* **2007,** 90, 252907.

[24] Y. Tian, L. Jin, H. Zhang, Z. Xu, X. Wei, E.D. Politova, S.Y. Stefanovich, N.V. Tarakina, I. Abrahams, H. Yan, *J. Mater. Chem. A*, **2016**, 4, 17279−17287.

[25] J.Gao, L. Zhao, Q. Liu, X. Wang, S. Zhang, J.F Li, *J. Am. Ceram. Soc.,* **2018**, 101, 5443−5450.

[26] L. Zhao, Q. Liu, S. Zhang, J.F. Li, *J. Mater. Chem. C*, **2016,** 4(36), 8380-8384.

[27] L. Zhao, J. Gao, Q. Liu, S. Zhang, J.F. Li, *ACS Appl. Mater. Interfaces*, **2018**, 10(1), 819-826.

[28] N. Luo, K. Han, L. Liu, B. Peng, X. Wang, C. Hu, H. Zhou, Q. Feng, X. Chen, Y. Wei, *J. Am. Ceram. Soc.*, **2019**, 102(8), 4640-4647.

[29] J. Gao, Q. Liu, J. Dong, X. Wang, S. Zhang, J.F. Li, *ACS Appl. Mater. Inter.*, **2020**, 12(5), 6097-6104.

[30] K. Han, N. Luo, Y. Jing, X. Wang, B. Peng, L. Liu, C. Hu, H. Zhou, Y. Wei, X. Chen, Q. Feng, *Ceram Int.*, **2019**, 45(5), 5559-5565.

[31] S. Mao, N. Luo, K. Han, Q. Feng, X. Chen, B. Peng, L. Liu, C. Hu, H. Zhou, F. Toyohisa, Y. Wei, *J. Mater. Sci-Mater. El.*, **2020**, 31(10), 7731-7741.

[32] S. Li, H. Nie, G. Wang, C. Xu, N. Liu, M. Zhou, F. Cao, X. Dong, *J. Mater. Chem. C*, **2019,** 7, 1551-1560.

[33] L. Zhao, Q. Liu, J. Gao, S. Zhang, J.F. Li, *Adv. Mater.*, **2017**, 29(31), 1701824.

[34] L. Yang, X. Kong, F. Li, H. Hao, Z. Cheng, H. Liu, J.F. Li, S. Zhang, *Progress in Materials Science,* **2019**, 102, 72–108

[35] G. Wang, Z. Lu, J. Li, H. Ji, H. Yang, L. Li, S. Sun, A. Feteira, H. Yang, R. Zuo, D. Wang, I.M. Reaney, *J. Eur. Ceram. Soc.*, **2020**, 40(4), 1779–1783.

[36] G. Wang, J. Li, X. Zhang, Z. Fan, F. Yang, A. Feteira, D. Zhou, D.C. Sinclair, T. Ma, X. Tan, D. Wang, I.M. Reaney, *Energy Environ. Sci.*, **2019**, 12, 582–588

[37] H. Liu, Z. Zhou, Y. Qiu, B. Gao, S. Sun, K. Lin, L. Ding, Q. Li, Y. Cao, Y. Ren, J. Sun, X. Xing, J. Chen, *Mater. Horiz.*, **2020**, 7, 1912–1918

[38] N. Luo, K. Han, F. Zhuo, L. Liu, X. Chen, B. Peng, X. Wang, Q. Feng, Y. Wei, *J. Mater. Chem. C*, **2019**, 7(17), 4999-5008.

[39] Z. Yan, D. Zhang, X. Zhou, H. Qi, H. Luo, K. Zhou, I. Abrahams, H. Yan, *J. Mater. Chem. A*, **2019**, 7(17), 10702-10711.

[40] C. Xu, Z. Fu, Z. Liu, L. Wang, S. Yan, X. Chen, F. Cao, X. Dong, G. Wang, *ACS Sustain. Chem. Eng.*, **2018**, 6(12), 16151-16159.

[41] Y. Xu, Y. Guo, Q. Liu, G. Wang, J. Bai, J. Tian, L. Lin, Y. Tian, *J. Eur. Ceram. Soc.*, **2020**, 40(1), 56-62.

[42] N. Luo, K. Han, F. Zhuo, C. Xu, G. Zhang, L. Liu, X. Chen, C. Hu, H. Zhou, Y. Wei, *J. Mater. Chem. A*, **2019**, 7(23), 14118-14128.

[43] T. Kumazawa, Y. Kumagai, H. Miura, M. Kitano, *Appl. Phys. Lett.*, **1998**, 72, 608.

[44] H. Zhu, D.P. Chu, N.A. Fleck, S.E. Rowley, S.S. Saxena, *J. Appl. Phys.*, **2009**, 105, 061609.

[45] R. Yimnirun, Y. Laosiritaworn, S. Wongsaenmai, *J. Phys. D: Appl. Phys.*, **2006**, 39, 759-764.

**Figure Captions**

Figure 1. Schematics of (a) a MLCC, and (b) the strain distribution in cross-section of a MLCC when it was exposed to a high electric field. Here, $t_{inactive}$ is the thickness of inactive dielectric ceramic layer, $t_{active}$ is the thickness of active dielectric ceramic layer, and $F$ is the force exerted on the active dielectric ceramic layer by the clamping from inactive layer. (c), Finite-element simulations for the distribution of strains with application of 10 V between two electrodes. (d) Review of the recoverable energy storage densities ($W_{re}$) and energy efficiency ($\eta$) reported for AgNbO$_3$ based energy storage materials.

Figure 2 (a) $P$-$E$ loops measured at 350 kV/cm, (b) breakdown field and (c) recoverable energy storage $W_{rec}$ for Ag(Nb$_{0.85}$Ta$_{0.15}$)O$_3$ multilayer capacitors, where the $t_{active}$ is 17 μm, 34 μm, 51 μm and 68 μm, respectively, (d) $P$-$E$ loops for the samples with $t_{active}$=17 μm, measured at different electric field, (e) apparent remanent polarization, $P_{r,apparent}$, obtained from the $P$-$E$ loops, and (f) leakage current density $J$ for samples with $t_{active}$=17 μm and 68 μm.

Figure 3 Effect of MnO$_2$ doping on $P$-$E$ loops, leakage current, resistance and dielectric properties of ANT capacitors. (a) $P$-$E$ loops measured at 450 kV/cm; (b) leakage current $J$, (c) temperature dependence of dielectric constant $\varepsilon_r$ and dielectric loss tan$\delta$, and (d) impedance spectroscopy measured at 500 °C for ANT and ANT+Mn capacitors.

Figure 4. Effect of $t_{inactive}$ on the P-E loop and energy storage density, (a) schematic of ANT+Mn capacitors where the $t_{active}$ was fixed at 22 μm; (b) P-E loop of ANT+Mn capacitors with different $t_{inactive}$; (c) the variation of $W_{rec}$ and $P_{max}$ as a function of $t_{inactive}$ for ANT+Mn capacitor; (d-f) the finite-element simulations, where the electric field between two electrodes is 250 kV/cm, and (g) the variation of average stress of active layer as a function of $t_{inactive}$.

Figure 5. Effect of $t_{active}$ on the P-E loop and energy storage density, (a) schematic of ANT+Mn capacitors where the $t_{inactive}$ was fixed at 33 μm; (b) P-E loop of ANT+Mn capacitors with different $t_{active}$; (c) the variation

of $W_{rec}$ and $P_{max}$ as a function of $t_{active}$ for ANT+Mn capacitor; (d-f) finite-element simulations (all active layers

are under 250 kV/cm), and (g) the variation of average stress of active layer as a function of $t_{active}$.

Figure 6.    Image and microstructures of ANT+Mn multilayer ceramic capacitor. a) Image of the as-prepared

ANT+Mn multilayer ceramic capacitors. b) Cross-sectional SEM image of the MLCC, and (c) EDS-SEM

images for the elemental distributions (Pt, Ag, O, and Ta).

Figure 7. TEM images of ANT+Mn multilayer capacitor: (a) Microstructure showing grains and grain

boundaries. (b) High resolution electron microscopy (HREM) image and selected-area electron diffraction

(SAED) pattern (insert), (c) EDS-TEM images for the distributions of specific elements (Ag, Nb, Ta and Mn).

Figure 8. Energy storage of ANT+Mn multilayer capacitors. (a) P-E loops of ANT+Mn multilayer capacitor

which can endure a high electric field of 1020 kV/cm, (b) P-E loops of ANT+Mn multilayer capacitor.